International Journal of Mass Spectrometry 308 (2011) 1–10

Contents lists available at ScienceDirect

International Journal of Mass Spectrometry

journal homepage: www.elsevier.com/locate/ijms

# A novel projection approximation algorithm for the fast and accurate computation of molecular collision cross sections (I). Method

Christian Bleiholder, Thomas Wyttenbach, Michael T. Bowers*

*Department of Chemistry and Biochemistry, University of California, Santa Barbara, CA 93106 - 9510, United States*

ARTICLE INFO

*Article history:*
Received 24 May 2011
Received in revised form 22 June 2011
Accepted 22 June 2011
Available online 2 August 2011

*Keywords:*
Ion mobility
Macromolecules
Collision cross section
Projection approximation

ABSTRACT

A projected superposition approximation (PSA) to compute molecular collision cross sections measured in ion-mobility experiments is developed. In the framework of the PSA, molecular collision cross sections are computed as a projection approximation modified to account for collective size and shape effects. Illustrative calculations on a range of molecular structures demonstrate that the PSA algorithm is able to handle the complex molecular shapes (concave, convex, pores, cavities, channels) as well as the range in molecular size typical to proteins. Our results indicate strong numerical agreement with the accurate trajectory method while only a small fraction of the computational demand is required.



## 1. Introduction

The use of ion mobility spectrometry–mass spectrometry (IMS–MS) for the structural characterization of small organic and inorganic molecules has a well-developed history [1–6]. Advancements in IMS–MS instrumentation over the last two decades have allowed the investigation of large, macromolecular biological compounds [7–21]. Of particular relevance here are the structural characterization of toxic oligomers in Alzheimer's peptide amyloid-β [22], the elucidation of self-assembly pathways of amyloid peptides [23], and viral capsids [24]. These applications highlight the tremendous potential of IMS–MS to the life science community by offering a unique combination of fast, sensitive and accurate determination of mass and structure of macromolecular biological complexes that is unmatched by any other analytical technique.

Unfortunately, the advances in the theory of ion mobility spectrometry have not progressed as rapidly. However, computational algorithms that relate model structures to cross sections for comparison with IMS–MS experimental cross sections are pivotal to successful application of IMS–MS [7,14,15,25]. Available algorithms [26–29] were designed with small organic and inorganic compounds in mind. Unfortunately, when extended to larger biologically relevant systems these existing algorithms are rendered either too inaccurate [26] by the complexity of the molecular shape of macroscopic biological compounds or computationally too demanding [27,29] due their sheer size. As a consequence, it is now possible to routinely record experimental ion mobility spectra for macroscopic biological compounds, but impossible to reliably connect the information contained in them to molecular structure [7,21].

Ion mobility spectrometry determines the ion mobility $K$ of an analyte ion in a drift cell filled with a buffer gas [30]. The mobility $K$ is defined as the ratio of $v_D/E$, where $v_D$ is the drift velocity of an ion in an applied linear electric field with strength $E$. The mobility is given by transfer of momentum between the analyte ion and the buffer gas. Using basic mathematical formulae, it is straightforward to derive a simple expression that relates the reduced ion mobility $K_0$ (normalized to 760 Torr and 273.15 K) to a molecular momentum transfer integral $\Omega$:

$$K_0 = \frac{3e}{16N_0}\sqrt{\frac{2\pi}{\mu kT}}\frac{1}{\Omega} \quad (1)$$

Here $e$ is the charge on the analyte, $N_0$ the number density at 760 Torr and 273.15 K and $T$ the temperature of the buffer gas. The central quantity in Eq. (1) is the molecular momentum transfer integral $\Omega$, which is determined by the scattering process between the buffer gas and the analyte. The momentum transfer integral $\Omega$ is the quantity that contains the information of the ion geometry. Therefore, $\Omega$ is exceedingly difficult to obtain rigorously for any but the simplest molecular systems because of the highly non-local and correlated nature of the van der Waals interaction [31–34] between the buffer gas and the analyte. These long-range interactions are attractive in nature and cause the well depth of the interaction potential to increase with increasing molecular size and atom

* Corresponding author. Tel.: +1 805 893 3049.
*E-mail address:* bowers@chem.ucsb.edu (M.T. Bowers).

1387-3806/$ – see front matter © 2011 Elsevier B.V. All rights reserved.
doi:10.1016/j.ijms.2011.06.014

density and make it a function of the molecular shape. It is these *size* and *shape effects* of the intermolecular interaction potential which make an accurate computation of ion mobilities from model structures difficult and time-consuming (for details see Section 2).

Here, we present the projected superposition approximation (PSA), a novel algorithm to compute molecular ion mobilities. It is explicitly designed to accurately account for size and shape effects while being computationally highly efficient. Its high accuracy and low computational demand make it specifically suited for the calculation of cross sections of biological compounds and other macromolecules. Additionally, we discuss and evaluate the performance of the PSA in terms of accuracy and computational demand in comparison with existing methods. The manuscript is organized such that the mathematically interested reader will find all important concepts presented in Sections 2, 3 and 5, while those who are more interested in the application of the PSA can skip directly to Section 6.

## 2. Theory

The central quantity in Eq. (1) is the molecular momentum transfer integral $\Omega$, which can be approximated by the orientationally averaged collision integral or cross section $\Omega^{(1,1)}$ under low-field conditions [30,35]. $\Omega^{(1,1)}$ can be expressed as

$$\Omega^{(1,1)}(T) = k \int_0^\infty d\varepsilon \int_0^\pi d\alpha f(\varepsilon, T)\sigma(\varepsilon, \alpha)(1 - \cos\,\alpha) \qquad (2)$$

Here $k$ is a normalization constant, $\alpha$ is the scattering angle, $f(\varepsilon, T)$ is the distribution of the kinetic energy $\varepsilon$ for a buffer gas with temperature $T$, and $\sigma(\varepsilon, \alpha)$ is the probability distribution of the deflection angle $\alpha$ for trajectories with kinetic energy $\varepsilon$. Note that $\sigma(\varepsilon, \alpha) = \int d\boldsymbol{r} \int d\boldsymbol{\varphi}\, \alpha(\varepsilon, \boldsymbol{r}, \boldsymbol{\varphi})$ is a six-dimensional volume integral as the deflection angle $\alpha(\varepsilon, \boldsymbol{r}, \boldsymbol{\varphi})$ of a trajectory with kinetic energy $\varepsilon$ depends on the relative position $\boldsymbol{r}$ and orientation $\boldsymbol{\varphi}$ of the analyte and the buffer atom. The quantity $\Omega^{(1,1)}(T)$ is the thermal average of the momentum transfer between the analyte ion and the buffer gas due to collisions in the drift cell at temperature $T$. The value of the integral $\sigma(\varepsilon, \alpha)$ can be obtained by solving the equations of motion $\mathcal{L}(p, q) = T(p) - V(q)$ (where $p$ and $q$ are the generalized momentum and coordinates, respectively) of the scattering process between the analyte and the buffer gas for a sufficiently large number of collision geometries on the scattering potential energy surface $V(q)$. For atomic ions, the scattering process is a two-body problem and evaluation of $\Omega^{(1,1)}$ is trivial. However, the scattering process of polyatomic ions in the drift cell is a many-body problem and exceedingly difficult to solve.

What changes on a qualitative level when going from a single atomic ion to a polyatomic ion is the complexity of the intermolecular interaction potential energy surface $V(q)$. This interaction potential $V(q)$ is determined by the intermolecular interaction operator $\hat{W} = H - H_{\text{ion}}$, where $H$ is the full intermolecular electronic Hamiltonian and $H_{\text{ion}}$ is the molecular Hamiltonian of the polyatomic analyte ion [31–33]. This interaction operator $\hat{W}$ causes the electrons of the buffer gas atom to *simultaneously* interact with each electron of the polyatomic analyte. It is pivotal for the current work to note that for this reason the interaction between the analyte and the buffer gas is *collective* in nature: the well of the interaction potential is (a) deepened with increasing number of atoms and (b) becomes dependent on the surface curvature of the polyatomic ion. For example, the average He–$C_{60}^+$ interaction was estimated to be eight times as strong as that of a single He–C interaction [26,27] and different to that of the He–Graphite potential [27].

The contribution of glancing collisions to the molecular momentum transfer is large for an atomic ion and negligibly small for macroscopic objects. However, in an intermediate size range (tens to thousands of atoms, see below), glancing collisions become increasingly important with increasing molecular size as a consequence of the deepened interaction potential. In other words, the effective atomic radius of a particular atom in the analyte increases due to its molecular environment. This will be denoted as the *size effect* in the course of this work. At the same time, the interaction potential depends on the curvature defined by the molecular geometry of the analyte. This effect is most dramatic for concave features of the analyte, such as cups, because here the deflection angle can become very large (i.e., 180° for a large number of collision geometries) and lead to a high momentum transfer [28]. We will refer to this as the *shape effect* and discuss its consequence at length in Section 6. At this point, we emphasize that the cause of both the size and shape effects is the simultaneous interaction of the buffer gas electrons with all electrons of the analyte. They are non-local (or collective) in nature and are generally coupled to each other.

How do current models account for these non-local effects? The most rigorous way to simplify the scattering problem is to approximate the scattering potential energy surface $V(q)$ by a sum of two-body interaction terms. The collision integral $\Omega^{(1,1)}$ can then be evaluated through the scattering angles $\alpha$ by solving $\mathcal{L}(p, q)$ numerically for a sufficiently large number of collision geometries. This procedure has been described by Jarrold and co-workers and is known as the trajectory method (TJM) [27]. In their TJM model, the scattering potential energy surface $V(q)$ is expressed as a superposition of atomic two-body interaction terms consisting of a Lennard–Jones and an ion-induced dipole term. The position and depth of the well $r_{\text{LJ}}$ and $\varepsilon_{\text{LJ}}$ of the Lennard–Jones (12,6) potential are fitted to experiment and are consistent with typical atomic parameters [27]. The beauty of this method is that the size and shape effects are intrinsically included within the model. Therefore, the TJM yields very accurate collision cross sections as long as the interaction potential $V(q)$ is well-represented by the sum of two-body interactions. However, this method is very time-consuming and for this reason cannot be applied to large biological compounds (see Supporting Information).

A further approximation can be introduced by simplifying the two-body interaction potential to that of the collision of hard spheres with defined collision radius $R_{\text{coll}}(T)$. The collision integral $\Omega^{(1,1)}$ can then be accessed via ray tracing of the scattered trajectories and deducing the corresponding collision angles $\alpha$. Shvartsburg and Jarrold introduced this as the exact hard-sphere scattering (EHSS) model, in which the polyatomic analyte is represented as a collection of spheres with defined collision radius $R_{\text{coll}}$ [28]. This model treats a collision as a two-body process with collision radius $R_{\text{coll}}$ independent of the number of spheres present (molecule size) and independent of the arrangement of the spheres (molecule geometry). The EHSS model therefore does not account for the size effect [29,36]. However, it does approximate the non-local shape effect through the allowance of multiple collisions within one trajectory.

The greatest simplification of the scattering process is achieved in projection approximation (PA) methods [26,37,38]. Here, the polyatomic ion is considered as collections of spheres with collision radius $R_{\text{coll}}$. The collision integral $\Omega^{(1,1)}$ is then evaluated as the orientation averaged area of the union of these spheres projected on a plane perpendicular to the axis of orientation. This model completely neglects both the size and shape effects and is entirely local in nature. Ultimately, within the limits of this model any details of the scattering process are considered not relevant for evaluating the collision integral $\Omega^{(1,1)}$. This method is computationally highly efficient but can also be highly inaccurate (errors approaching 30% are detected in this work; see Section 6 for details). The classical PA model [28,38] has been significantly improved by correcting the size effect empirically for molecules up to 200 atoms [39,40]

allowing accurate cross sections for many relatively small molecular systems to be determined. Here we will be dealing with both much larger systems and more complex surfaces requiring a much more sophisticated approach.

## 3. Method

Our goal here is to develop an algorithm that accounts accurately for the non-local size and shape effects while being computationally highly efficient. We avoid the extremely time-consuming numerical approach taken by the TJM of solving the equations of motions. Instead, we choose to first identify the pitfalls in the PA method and then show how they can be circumvented without compromising the simplicity of the method.

Within the general framework of the PA, the momentum transfer integral or collision cross section $\Omega^{(1,1)}(T)$ is approximated by the following numerical procedure [26,38]. The molecule is repeatedly projected onto randomly chosen planes $\mathcal{P}_i$ in space, and represented by a collection of circles with defined radius $R_{\mathrm{coll}}(T)$ on the plane. The circles are located at the positions of the atoms projected on plane $\mathcal{P}_i$. To this end, the radius $R_{\mathrm{coll}}(T)$ is approximated by atom–atom collision integrals $\omega_j^{(1,1)}$ between a particular atom $j$ of the analyte and the scattered helium atom as $R_{j,\mathrm{coll}}(T) = \sqrt{\omega_j^{(1,1)}/\pi}$ [26,30]. Then the collision cross section $\Omega_i$ perpendicular to $\mathcal{P}_i$ is set to the area on plane $\mathcal{P}_i$ that is enclosed by the collection of the circles. As a result, the momentum transfer integral $\Omega^{(1,1)}(T)$ is approximated as the orientation average ($\Omega$) of the projection areas $\Omega_i$ on a large number of randomly chosen planes $\mathcal{P}_i$

$$\Omega^{(1,1)}(T) \equiv \langle\Omega\rangle = \frac{1}{n}\sum_{i=1}^{n}\Omega_i \tag{3}$$

We highlight two important aspects of the above procedure. The first point here is that the complex scattering process between the buffer gas atom and the polyatomic ion is approximated as that of isolated atom–atom interactions by writing $R_{j,\mathrm{coll}}(T) = \sqrt{\omega_j^{(1,1)}/\pi}$. This is incorrect and ignores the *simultaneous* interaction of the buffer gas atom with all atoms of the analyte. As pointed out [27], this is of particular relevance for low temperatures. Second, all shape information of the molecule normal to the plane $\mathcal{P}_i$ is lost during the projection. In particular, the projection of the molecule on a plane $\mathcal{P}_i$ renders concave and convex features of the molecule identical. Also this is incorrect (e.g., looking down into an open cup versus looking down onto the lid of a covered cup). This simplification ignores the significantly different distribution of deflection angles of concave and convex molecular geometries [28]. Consequently, the standard PA approach yields cross sections that are often significantly too small for large molecules with complex shape [28].

## 4. Projected superposition approximation (PSA)

With the projected superposition approximation (PSA) model, we choose to retain the overall concept of the PA due to its simplicity and high computational efficiency. However, we approximate the molecular momentum transfer integral $\Omega^{(1,1)}(T)$ as an orientation averaged projection area $\langle\Omega_{\mathrm{PSA}}\rangle$ multiplied by a shape factor $\rho$:

$$\Omega^{(1,1)}(T) \equiv \Omega_{\mathrm{PSA}}^{(1,1)}(T) = \langle\Omega_{\mathrm{PSA}}\rangle \cdot \rho \tag{4}$$

Here the orientation averaged projection area $\langle\Omega_{\mathrm{PSA}}\rangle$ accounts for the size effect. Any deviation of the molecular shape from full convexity is then corrected by the shape factor $\rho$.

### 4.1. Projection area $\langle\Omega_{\mathrm{PSA}}\rangle$: size effect

The projection area $\Omega_i$ of the analyte on plane $\mathcal{P}_i$ is typically computed in a Monte Carlo fashion by randomly picking points $\boldsymbol{x}$ in the plane within an area $A_i$ that encloses the collection of circles representing the analyte [38,41]. If point $x \in \mathcal{P}_i$ lies within any one circle with radius $R_{j,\mathrm{coll}}(T)$, it is denoted as a "hit". The projection area $\Omega_i$ is then approximated by the area $A_i$ multiplied by the ratio of hits to the total number of points picked.

The important question here is how to decide whether a point $x \in \mathcal{P}_i$ belongs to the analyte. In the PSA we replace the concept of an atomic hard-sphere radius with an atomic collision probability $p_j(T, \boldsymbol{x})$ (see Fig. 1B). The quantity $p_j(T, \boldsymbol{x})$ is the probability of a collision between the buffer gas atom and a particular atom $j$ within the polyatomic analyte at point $\boldsymbol{x} \in \mathcal{P}_i$. Obviously, $p_j(T, \boldsymbol{x})$ depends on the distance $r = |\boldsymbol{x} - \boldsymbol{r}_j|$ of a point $\boldsymbol{x} \in \mathcal{P}_i$ to the position $\boldsymbol{r}_j$ of atom $j$ and decreases monotonously with increasing values of $r$. We therefore choose $p(T, \boldsymbol{x})$ to take on the functional form (see Section S1.3 in the Supplementary Information for details):

$$p_j(T, \boldsymbol{x}) = \begin{cases} 1, & r \le q_{j,\mathrm{coll}}(T; r_{\mathrm{LJ}}, \varepsilon_{\mathrm{LJ}}) \\ \alpha e^{-(r-q_{j,\mathrm{coll}})k_1 \cdot T^{l_1}} + (\alpha - 1)e^{-(r-q_{j,\mathrm{coll}})k_2 \cdot T^{l_2}}, & r > q_{j,\mathrm{coll}}(T; r_{\mathrm{LJ}}, \varepsilon_{\mathrm{LJ}}) \end{cases} \tag{5}$$

Here $r = |\boldsymbol{x} - \boldsymbol{r}_j|$ and $q_{j,\mathrm{coll}}(T; r_{\mathrm{LJ}}, \varepsilon_{\mathrm{LJ}}) = \sqrt{\omega_j^{(1,1)}/\pi}$ is the atomic collision radius of atom $j$ defined by the momentum transfer integral $\omega_j^{(1,1)}$ of an isolated atom colliding with a buffer gas particle $X$. The $X$–$j$ interaction can be approximated by a (12,6,4) potential using established atom–atom Lennard–Jones parameters $r_{\mathrm{LJ}}$ and $\varepsilon_{\mathrm{LJ}}$ (well position and depth, respectively) [26,30]. The parameters $k$ and $l$ reflect the strength and the temperature-dependency of the decreasing collision probability with increasing distance $r$ from the atomic center of atom $j$. The functional form of a double exponential decay can be rationalized by the properties of the Lennard–Jones potential which fundamentally governs the scattering process. At short distances $r$, the Lennard–Jones potential decays very steeply and does not have much additive character. However, the Lennard–Jones potential is still significant at large distances $r$ and the strength of the interaction is very sensitive to a superposition of several Lennard–Jones functions. At least a double exponential form of the decay is necessary to allow the flexibility of both properties of the Lennard–Jones potential.

A point $\boldsymbol{x} \in \mathcal{P}_i$ is then defined to contribute to the PSA projection area $\Omega_{\mathrm{PSA},i}$ if the superposition of all atomic probabilities $p_j(T, \boldsymbol{x})$ is greater than a randomly chosen value $v$ between 0 and 1 (Monte Carlo criterion). Hence, if the cumulative collision probability $\mathcal{P}(T, \boldsymbol{x})$ of a system with $m$ atoms

$$\mathcal{P}(T, \boldsymbol{x}) = \sum_{j=1}^{m} p_j(T, \boldsymbol{x}) \tag{6}$$

is larger than $v$ the point $\boldsymbol{x}$ contributes to the PSA cross section ("hit"), otherwise it does not ("miss"). As a result, the orientation averaged projection area $\langle\Omega_{\mathrm{PSA}}\rangle$ becomes an orientation averagedfunctional of the superposition of atomic collision probabilities

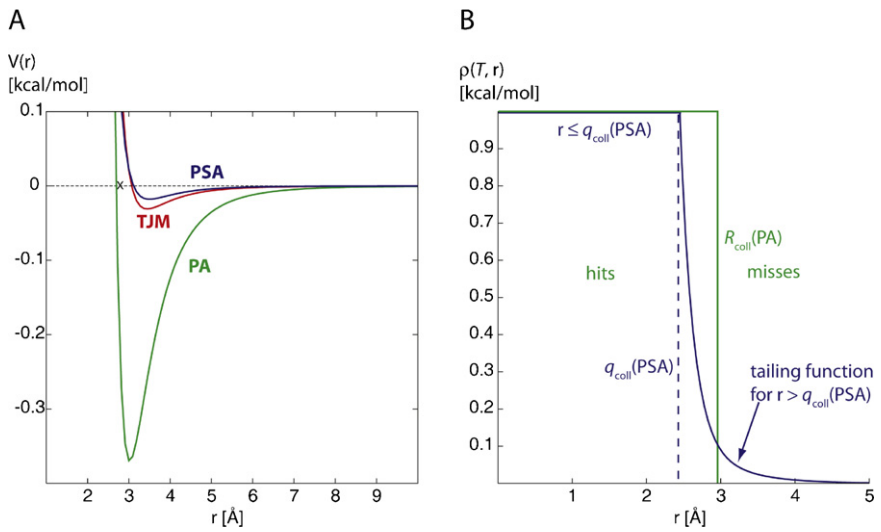


**Fig. 1.** (A) Lennard–Jones (12,6) potential fitted for the TJM, PA and PSA models. The fitted PA potential amounts to the full He–$C_{60}$ potential and parameterizes the size effect in $C_{60}$ for this model. The PSA and TJM agree well with the atomic He–C potential and describe the shape and size effects within these models. (B) The concept of a hard-sphere collision of the PA model ("hits', "misses") is compared to that of the atomic collision probability $p_j(T, \boldsymbol{x})$ for the PSA model.

$\mathcal{P}(T, \boldsymbol{x})$:

$$\langle \Omega_{\mathrm{PSA}} \rangle = \frac{1}{n}\sum_{i=1}^{n} \Omega_{i,\mathrm{PSA}} = \frac{1}{n}\sum_{i=1}^{n} \tilde{\Omega}_i[\mathcal{P}(T, \boldsymbol{x})]$$

$$= \frac{1}{n}\sum_{i=1}^{n} \tilde{\Omega}_i \left[\sum_{j=1}^{m} p_j, (T, \boldsymbol{x})\right] \quad (7)$$

Here we have introduced the projected superposition approximation cross section of a specific orientation $\Omega_{i,\mathrm{PSA}}$ as a functional of the cumulative collision probability $\mathcal{P}(T, \boldsymbol{x})$ which is in turn a function of $p_j(T, \boldsymbol{x})$. Note, that $\mathcal{P}(T, \boldsymbol{x})$ depends on the positions of all atoms of the analyte (Eq. (6)). Consequently, $\langle \Omega_{\mathrm{PSA}} \rangle$ accounts for the simultaneous interaction of the buffer gas atoms with all atoms of the analyte ion.

### 4.2. Shape factor ρ(T): molecular concaveness

The orientation averaged projection area $\langle \Omega_{\mathrm{PSA}} \rangle$ as defined above is an average of areas projected into randomly chosen planes and accounts for molecule size and shape to some degree (spherical, planar, elongated). However, more subtle shape information is lost in $\langle \Omega_{\mathrm{PSA}} \rangle$. For instance, differentiation between scattering off a concave and a convex surface is not accounted for.

In any projection approximation, information about concave "dents" in an object is lost. However, the exact nature of the surface does have an effect on momentum transfer in collisions, with dents increasing momentum transfer on average compared to the corresponding dent-free convex surface [28]. Therefore, the overall degree of concaveness of the polyatomic ion must be evaluated in order to improve the $\langle \Omega_{\mathrm{PSA}} \rangle$ value. Here we chose the ratio

$$\rho = \frac{A_{\mathrm{mol}}}{A_{\mathrm{ce}}} \quad (8)$$

of the effective molecular surface area $A_{\mathrm{mol}}$ to the area $A_{\mathrm{ce}}$ of the convex envelope of the molecule as shape factor to describe the degree of molecular concaveness. The QuickHull algorithm [42] is used to compute the convex envelope. We apply alpha-shape theory [43–45] to generate the molecular surface [46] and chose a graph-theoretical approach to identify invisible patches on the surface to compute the effective molecular surface area $A_{\mathrm{mol}}$. The key point here is to identify the fraction of the molecular surface that effectively takes part in collisions with the buffer gas. The interested reader is referred to the Supplementary Information, Section 1.4, for a detailed description of the shape factor. We emphasize that no statistical fitting procedure was applied to the shape factor in this work, which would improve the performance of the PSA model. This will be done in a future publication that includes parameters for other elements (i.e., hydrogen, oxygen, nitrogen).

## 5. Parameterization

The carbon parameters used in this work for the PSA model were optimized by a Monte Carlo procedure as follows. The TJM cross sections $\Omega_{\mathrm{TJM}}$ $(T)$ for $C_{60}$, $C_{180}$, $C_{540}$, $C_{d,51}$, $C_{d,214}$ and $C_{d,1006}$ (see Figs. S5 and S6 in the Supplementary Information) were computed by the TJM in the temperature range from $T = 80$ K to $T = 700$ K in steps of 30 K. Then the function $S(r_{\mathrm{LJ}}, e_{\mathrm{LJ}}, \alpha, k_1, k_2, l_1, l_2)$ with

$$S(r_{\mathrm{LJ}}, e_{\mathrm{LJ}}, \alpha, k_1, k_2, l_1, l_2) =$$

$$\frac{1}{n}\sum_{i}^{n}\frac{1}{m}\sum_{T}^{T_m}\left[\frac{\Omega_{\mathrm{PSA},i}(T, r_{\mathrm{LJ}}, e_{\mathrm{LJ}}, \alpha, k_1, k_2, l_1, l_2) - \Omega_{\mathrm{TJM},i}(T)}{\Omega_{\mathrm{TJM},i}(T)}\right]^2 \quad (9)$$

was minimized in a Monte Carlo manner, where the summation is taken over all $n$ compounds and $m$ temperatures ($T = 80$ K, 110 K, . . ., 700 K). A new parameter set $\{r_{\mathrm{LJ}}, e_{\mathrm{LJ}}, \alpha, k_1, k_2, l_1, l_2\}_{\mathrm{new}}$ was derived by randomly selecting a specific parameter and randomly changing its corresponding value within a specified step size. To this end, the parameter to be modified was drawn from a one dimensional Sobol sequence [47,48] for improved sampling performance and the corresponding step value was determined by a 64-bit Mersenne Twister [49]. A new parameter set, $\{r_{\mathrm{LJ}}, e_{\mathrm{LJ}}, \alpha, k_1, k_2, l_1, l_2\}_{\mathrm{new}}$, was accepted if the Monte Carlo criterion $p < e^{-((S_{\mathrm{new}} - S_{\mathrm{old}})/\tau)}$ was fulfilled. The "temperature parameter", $\tau$, was varied throughout the optimization from 0.05 to 0.02 and $p$ was drawn from a 64-bit Mersenne Twister in the unit interval. A total of ca. 2,000,000 Monte Carlo steps were performed until the final parameter set was considered accurate enough for the purpose of this work. The resulting parameters are $r_{\mathrm{LJ}} = 3.495$ Å, $e_{\mathrm{LJ}} = 0.0177$ kcal/mol, $\alpha = 0.856$, $k_1 = 0.15835$, $k_2 = 0.15179$, $l_1 = 0.62905$, $l_2 = 0.43198$ (see also Section S1.5 in the Supporting Information).

Fig. 1 compares the optimized atomic carbon-helium interaction potentials $V(r; r_{\mathrm{LJ}}, e_{\mathrm{LJ}})$ for the TJM, PA and PSA models. The

parameters of the PA model reflect the molecular potential of $C_{60}$ [26], while those of the TJM agree with experimental atomic parameters [27]. Clearly, the atomic parameters optimized for the PSA model agree closely with the atomic TJM parameters. This is an important result, because it demonstrates that the tailing function in Eq. (5) correctly treats the superposition of atomic potentials.

### 5.1. Parameterization of PA and EHSS methods

PA and EHSS methods have previously been described [26,28]. In the implementation of those methods in the current work, the atomic collision radius $R_{coll}$ $(T)$ is chosen equal in both models for direct comparison. In addition, since the magnitude of $R_{coll}$ $(T)$ is given by atomic collision cross sections evaluated on the basis of atom–atom interaction potentials [26], the atomic collision radius $R_{coll}$ $(T)$ decreases with increasing temperature, both in our PA and EHSS models. In other words, since glancing collisions are less important at higher temperature the effective radius of the hard spheres decreases with increasing temperature. Therefore, both PA and EHSS cross sections of polyatomic systems become temperature dependent, too, even though the projection (PA) or scattering (EHSS) occurs for a collection of hard spheres with fixed collision radius $R_{coll}$ $(T)$.

## 6. Illustrative calculations

Our goal here is to demonstrate the performance of the projected superposition approximation (PSA) algorithm introduced in this work and compare it to the established trajectory (TJM), exact hard sphere scattering (EHSS) and projection approximation (PA) methods on three different sets of model compounds. For simplicity, we assume that a model agrees with the TJM data if the mutual deviation is less than 3%, i.e., lie within the shaded area in the figures.

The three sets of molecules are chosen such that the influence of the size and shape effects (see Section 2) on the performance of the computational methods can be separately discussed. The first set of molecules is comprised of solid and hollow spherical carbon clusters of varying sizes. These molecular systems are fully convex and the shape effect can therefore be neglected here. The second data set consists of cups derived from spherical carbon clusters. These geometries include concave geometries and both size and shape effects need to be considered. This set is of special importance, because the PA model was previously shown to be inaccurate for these geometries [28]. The third data set is comprised of carbon clusters with the geometrical complexities and sizes typical of proteins. This represents an illustration of the performance of the various methods for shapes and sizes typical to life science application.

## 7. Solid and hollow spherical carbon clusters: the size effect

### 7.1. Fullerenes $C_{60}$ to $C_{960}$

Figs. 2 and S6 (see Supporting Information Section S2) display the collision cross sections of the fullerenes [26,50] $C_{60}$ to $C_{960}$ as a function of temperature. Experimental $C_{60}$ collision cross sections were reported by different groups [27,51] and used to fit parameters for the TJM and PA models [26–28]. Consequently, we note only minor deviations among the various computational and experimental data for $C_{60}$. Overall, the agreement between the different data sets is generally better than the 3% error margin considered in this work.

No experimental results are available for the larger carbon clusters $C_{180}$ to $C_{960}$ and we consider the TJM results to be the most accurate data set (see Section 2). The effect of increasing molecular size is clearly observed in a significant increase in collision cross sections when going from $C_{60}$ to $C_{180}$, $C_{240}$, $C_{540}$ and $C_{960}$. The PSA and TJM models agree with one another within the 3% error margin over the whole temperature range studied for all fullerenes. This demonstrates the appropriate treatment of the size effect by the PSA algorithm through Eqs. (5) and (6).

However, we note that the collision cross sections predicted by the EHSS and PA models clearly deviate from the TJM data. For $T = 80$ K we observe cross sections ca. 10% smaller than predicted by the TJM. The neglect of the size effect by the PA model is visible in the PA data: the PA data increasingly underestimate the TJM data with increasing molecular size when going from $C_{60}$ to $C_{960}$. The performance of the EHSS model is more complex to analyze. We note an underestimation of the TJM data of approximately 10% at low temperature, exactly as the PA model. With increasing temperature the EHSS cross sections first approach and then surpass those predicted by the TJM. We note a crossing of the EHSS and TJM cross sections at $T \approx 400$–$500$ K, and between $T = 250$ K and $T = 500$ K the EHSS model appears to agree with the TJM.

Inconsistencies of the EHSS method for compounds with smooth molecular surfaces were reported earlier and rationalized by stronger size and shape effects for compounds with smaller interatomic distances [29,36]. To investigate the role of multiple collisions to our data in Fig. 2, we removed the effect of multiple collisions on the EHSS collision cross section (EHSS(sc) model in Fig. 2, see also Supporting Information Section S1 for the mathematical details). Interestingly, the EHSS(sc) model agrees very well with the PA data for the whole temperature range studied for all fullerenes $C_{60}$ to $C_{960}$. The effect of multiple collisions is therefore negligible at $T = 80$ K and successively increases to ca. 3% for $T = 700$ K for the larger fullerenes $C_{540}$ and $C_{960}$. This suggests that the EHSS cross sections approach those of the TJM with increasing temperature due to erroneous multiple collisions caused by an increased surface roughness particular to the EHSS model. This, however, is an effect of molecular shape, and indicates that the superior performance of the EHSS over the PA model for the larger fullerenes results from a cancellation of errors, but not from a physically correct description of the intermolecular scattering process: the increasing degree of diffuse scattering occurring off a collection of spheres in EHSS progressively increases the cross section with increasing fullerene size as a function of temperature.

### 7.2. Solid and hollow diamond-like spheres

Fig. S6 (see Supporting Information Section S2) displays the collision cross sections of solid and hollow spherical carbon clusters with a diamond lattice of equivalent diameter to the fullerenes $C_{60}$ to $C_{960}$ as a function of temperature. Again, no experimental results are available and we consider the TJM results to be the most accurate data set. Only the PSA model consistently agrees with the TJM data over the whole temperature range studied for all solid and hollow clusters $C_{d,51}$ to $C_{d,2350}$. Both the PA and EHSS data deviate systematically from the TJM data for the solid and hollow diamond-lattice clusters $C_{d,51}$ to $C_{d,2350}$ (see Fig. S6, Supporting Information). The PA cross sections of the solid and hollow diamond-lattice clusters are similar to that of the fullerene of equivalent size. This reflects the nature of the projection method which ignores any internal molecular structure. Consequently, the PA model overestimates the cross sections for solid $C_{d,51}$ with a smaller atom density than that of the $C_{60}$ fullerene, while it increasingly underestimates the cross sections for the larger solid lattice clusters $C_{d,1006}$ and $C_{d,2350}$. Similar results are observed for hollow $C_{d,51}$ to $C_{d,2350}$. These deviations clearly demonstrate the problems of the PA model and predict significant shortcomings of the PA model for large molecules with complex shape. The EHSS data in Fig. S6 (Support-

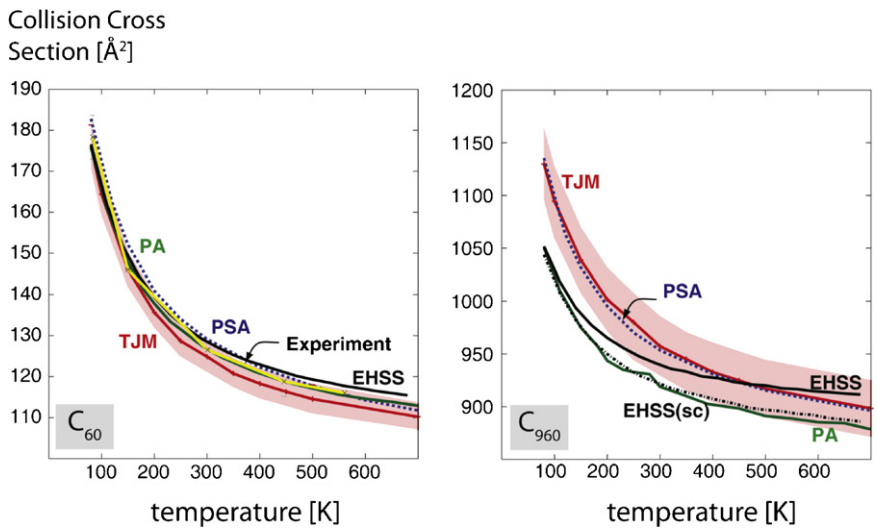


**Fig. 2.** The collision cross sections of $C_{60}$ (left) and $C_{960}$ (right) as a function of temperature. Only the TJM and PSA methods are capable of accounting for the difference in the intermolecular interaction potential between $C_{60}$ and $C_{960}$. EHSS(sc) in the dashed line.

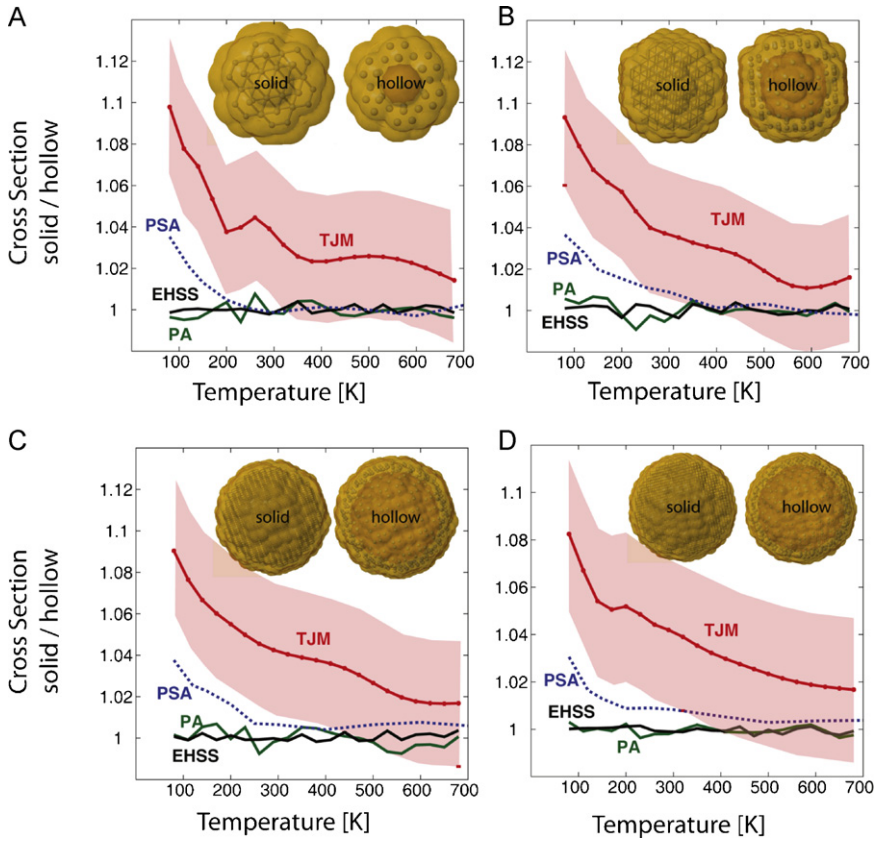


**Fig. 3.** Ratio of cross sections for solid and hollow diamond-like spherical carbon clusters. Only the TJM and PSA models account for the difference in cross section due to internal structure of the solid clusters.

ing Information) agree well with the PA data at lower temperature for all diamond lattice clusters $C_{d,51}$ to $C_{d,2350}$. This again demonstrates the failure of the EHSS to account for the size effect in an appropriate manner. Similar to the fullerene data, multiple collisions significantly affect the EHSS cross sections with increasing temperature. The good agreement of the EHSS cross sections for the solid and hollow diamond lattice clusters $C_{d,51}$ to $C_{d,2350}$ demonstrates that the EHSS mode fails to reflect the internal structure of the analyte.

The consideration of internal structure by the different methods is analyzed in Fig. 3, which depicts the ratio of cross sections for solid and hollow diamond-like spherical carbon clusters $r = \Omega_{solid}/\Omega_{hollow}$. The TJM data show a cross section consistently larger for the solid clusters than for the hollow clusters. The effect of internal structure on the collision cross section is estimated to be ca. 10% at low temperature by the TJM data. This effect diminishes with increasing temperature to about 2% at high temperature. The PSA model qualitatively reproduces this trend and predicts the

solid clusters to be larger than the hollow ones by a factor of ca. 4% at low temperatures and to a lesser extent at high temperatures. While we note that the PSA and TJM models disagree from one another on a numerical level, we emphasize that the PA and EHSS models fail to reproduce the TJM data even on a qualitative basis and do not predict any effect of internal structure on the cross section.

We conclude from the overall very good agreement of the PSA and TJM data that only the PSA method appropriately accounts for the size effect in a physically appropriate manner. Our above analysis shows that both the PA and EHSS models fail completely in describing the effect of increasing molecular size and internal structure in the fullerenes $C_{60}$ to $C_{960}$ and solid, hollow diamond-lattice clusters $C_{d,51}$ to $C_{d,2350}$. We note that the EHSS data are in better agreement with the TJM data for the larger molecules at $T \sim 300$ K than the PA data due to an unphysical shape effect caused by multiple collisions in the EHSS model.

## 8. Spheres and cups of carbon clusters $C_{60}$, $C_{180}$, $C_{240}$, $C_{960}$

The collision cross sections for the cups of the fullerenes $C_{60}$ to $C_{960}$ are given in Figs. 4 and S9 and S10 (see Supporting Information Section S3) as a function of temperature. Again, no experimental results are available and we consider the TJM results to be the most accurate data set. Several trends emerge that demonstrate how the various models treat molecular shape.

First, the PSA data agree well with the TJM data for the cups of $C_{60}$ to $C_{960}$ and shows an error distribution with respect to the TJM model with a maximum at 1.3% and a 0.9 quantile of 5.1%. This strong agreement with the TJM data further highlights the sound physical appropriateness of the PSA model to account for molecular shape and size. The PA data disagree with the TJM data for any molecular geometry with a significantly concave shape, except the structures derived from $C_{60}$. The deviation from the TJM data is largest for the shapes with largest degree of concavity within each data set of $C_{60}$, $C_{180}$, $C_{240}$ and $C_{960}$, in line with previous results [28]. Furthermore, we note that the peak deviation to the TJM data increases with increasing molecular size. The error distribution with respect to the TJM model shows a maximum at 3.4% and a 0.9-quantile of ca. 11%. These observations agree with previous reports [28,52] that the PA model is increasingly unable to reliably predict collision cross sections for larger molecules with non-convex shapes. Consequently, the PA model is particularly unsuited to compute cross sections for any biologically relevant compound.

Our data show that the performance of the EHSS model is again very complex. The EHSS model again overestimates the TJM data for the $C_{60}$ cups, due to the effect of multiple collisions. For the convex shapes derived from $C_{180}$, $C_{240}$ and $C_{960}$ the EHSS data underestimate the cross sections at low temperature while at high temperature it overestimates the TJM cross section. Again, multiple collisions contribute significantly to the EHSS cross sections. The EHSS method leads to a correct description of molecular shape only for highly concave structures. For example, multiple collisions correctly result in an increase in cross section of over 20% for the highly concave semi-sphere of $C_{960}$. However, the EHSS model overestimates the collision cross section for the successively smaller cups of $C_{180}$, $C_{240}$ and $C_{960}$ with a highly opened face and less concave shape due to multiple collisions. Hence, we conclude that the EHSS treatment of molecular shape and size leads to accurate cross sections only for strongly concave geometries. We further note a dependency of this behavior on molecular size. These observations clearly demonstrate that the EHSS model fails to account for molecular shape and size in a physically appropriate manner.

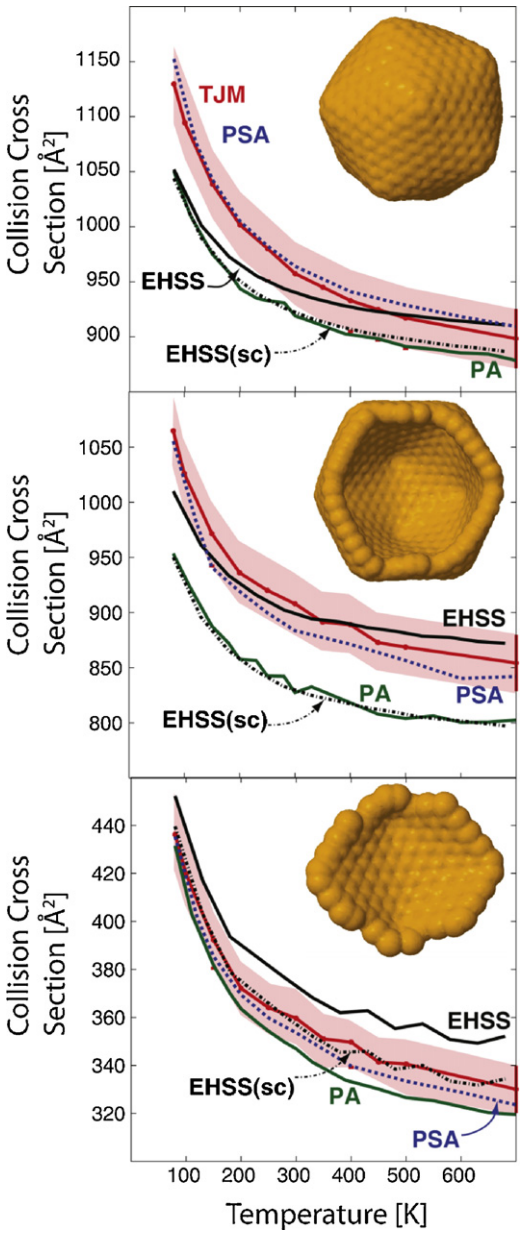


**Fig. 4.** Temperature-dependent cross sections of $C_{960}$ and two cups with shapes of varying concavity. Only the PSA model is able to reproduce the TJM data for all shapes. Specifically, the EHSS only performs well for the most concave shape.

## 9. Protein shapes

Finally, we sought to demonstrate the ability of the PSA model to predict cross sections for sizes and shapes common to biological macromolecules using a set of protein entries downloaded from the protein data bank (PDB). We replaced heavy elements by carbon and also removed hydrogen atoms from each PDB entry, because only the carbon parameters of the TJM were derived from temperature-dependent experimental data and subject to rigorous examination. Although this might seem somewhat arbitrary, we point out that hydrogen atoms are often removed from PDB structures when computing collision cross sections and that current algorithms use identical parameters for carbon, nitrogen and oxygen. Figs. 5 and S11 compare the performance of the PA, EHSS and PSA models to the TJM for selected protein shapes with 409–11,284 heavy atoms. These compounds were selected for their complex shapes (see Fig. S11 in the Supporting Information) which include

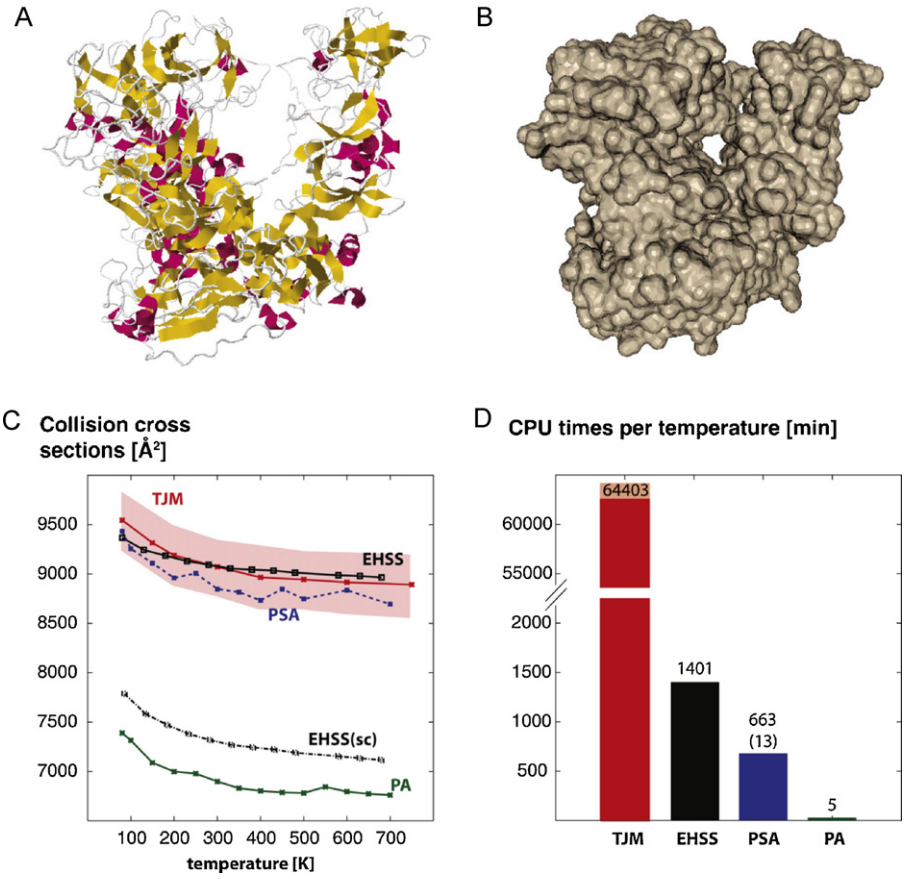


**Fig. 5.** (A) X-ray crystallographic structure of the Norwalk virus capsid (asymmetric unit). (B) Molecular surface of the of the corresponding all-carbon representation ($\alpha = 1.25$). (C) Temperature-dependent cross sections computed by the various methods. The PSA and EHSS models agree well with the TJM data. Notably, the PA method underestimates the TJM data by approximately 30%. (D) CPU time required for the calculations of each data point by the different methods for each temperature (see text for details).

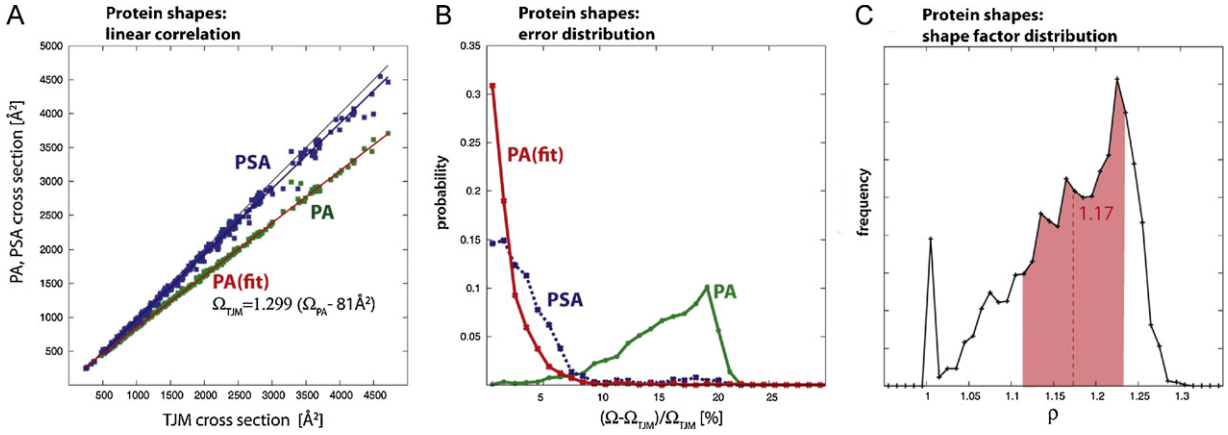


**Fig. 6.** (A) Correlation between TJM and PA (PSA) cross sections for protein shapes. The PA data can be fit to a straight line for the protein shapes with good accuracy. (B) Error distribution of the PA, PSA and fitted PA models for protein shapes. Notably, the most likely error of the PSA model is 2.8%. The error in the PA model is reduced from 21% to <2% by the fit. (C) Distribution of the shape factor $\rho$ for protein shapes. The average shape factor ($\langle \rho \rangle = 1.17$) and the ±5% intervals are indicated. Cross sections range from ca. 100–4500 Å$^2$ and the temperature from 80 K to 700 K in all plots.

deep cavities, pores, helices, channels and strongly concave molecular parts in addition to strong local surface roughness. As an example, Fig. 5A displays the structure of the asymmetric unit of the Norwalk virus capsid with 11,284 heavy atoms (PDB entry 1IHM). The corresponding molecular surface, used to compute the shape factor for 1IHM can be found in Fig. 5B.

The results for the various models are given in Fig. 5C. Clearly, the PA model fails to reproduce the TJM data even on a qualitative basis. The PA data are consistently smaller than the TJM data, with deviations approaching almost 30% for the larger shapes 1IHM and 1P1X (see Figs. 5 and S12 in the Supporting Information). This result indicates that the simple PA model without regard of the size and shape effects is unsuited to compute cross sections for complex molecules. The EHSS model performs very well for these rough protein shapes. This is in contrast to the molecular geometries discussed earlier, but in line with previous reports on Si clusters with rough surfaces [29]. We note that the EHSS(sc) data are roughly 10% larger than the PA data for the protein shapes in Figs. 5 and

S11, also in contrast to our data discussed in the previous sections. The difference between the PA and the EHSS(sc) data indicates that the scattering process off these molecular shapes takes on a substantial diffuse character, reflecting the strong roughness of the protein surfaces. For these rough shapes, multiple collisions take on a pivotal role during the scattering process and are necessary to correctly compute collision cross sections. As a consequence, the EHSS data are in good agreement with those of the TJM. This situation is very different from the molecules discussed earlier. The molecular surface was rather smooth in those cases and considering a molecule as a collection of hard spheres overestimated the contribution of multiple collisions to the collision cross section. However, actual proteins with hydrogen atoms included in their molecular structure may have a significantly smoother surface and it is therefore not clear how the EHSS model would perform in that instance. We are currently in the process of obtaining experimental data on systems that will allow accurate parameterization of the helium–hydrogen interaction potential. This work will be presented in a future publication.

The PSA data agree with the TJM data for all protein shapes depicted in Figs. 5 and S12. This strong agreement between the PSA and TJM data is especially noteworthy, because the compounds studied cover a huge range in molecular size and shape. For example, entry 1C58 is a protein that consists of four pores and entry 1DPL is shaped as a helix (see Fig. S11). Also, we emphasize that our PSA model is able to achieve numerical agreement with protein shapes approaching 10,000 Å$^2$ in cross section. Clearly, the PSA model can handle the difficult landscapes and sizes typical to proteins. We conclude that the shape factor as implemented in the current work is able to correctly recover molecular shape information which is lost during the projection nature of the PSA, even for the complex shapes and sizes typical to proteins.

## 10. Comparison of CPU time demand

Figs. 5D and S14 (see Supporting Information Section S4 for details) compare the CPU time demand of the PA, PSA and EHSS models over the TJM for the compounds studied in this work. Clearly, the TJM requires the most and the PA method the least CPU time. As an example, a PA calculation takes ca. 5 min and the TJM calculation roughly 47 days for PDB entry 1IHM with 11,284 heavy atoms as shown in Fig. 5D. The EHSS and PSA models require ca. 1401 and 663 min, rendering these two methods ca. 46 and 97 times faster than the TJM. The projection part of the PSA model takes about 13 min and is comparable in terms of computational demand to the PA model. It should be considered when interpreting the data that the PA and TJM executables were highly compiler optimized (Fortran programming language) whereas the EHSS and PSA were implemented in the Java programming language which is inefficient in numerical applications. Also, the PSA and EHSS cross sections were computed with much higher accuracy than the TJM data for 1IHM, which were aborted after 900,000 trajectories due to the prohibitive CPU demand required to achieve higher accuracy (see Fig. S13 in the Supporting Information). Accurate TJM data were obtained for the smaller proteins and carbon compounds in this study, and in those cases we observed the PSA model was ca. 900 times as fast as the TJM model. This value should be considered as a lower limit on the true value.

## 11. Error analysis of the PSA and PA data for protein shapes

We note a strongly linear correlation between the TJM and the PA and PSA cross sections for the protein shapes we analyzed as shown in Fig. 6A. Please note that the temperature range from 80 K to 700 K was included in this plot. A linear regression of the PA data yields the fit $\Omega_{TJM} = 1.299(\Omega_{PA} - 81\,Å^2)$ with $r^2 = 0.997$. Fig. 6B shows the error distribution of the PA, PSA and PA(fit) cross sections relative to those of the TJM. A maximum of the PSA and PA distributions is found at ca 3% and 20% relative deviation. Given the error of the TJM data, this indicates that the PSA model agrees with the TJM data. The strong deviation of ca. 20% of the PA model indicates that it is completely inappropriate to estimate collision cross sections for protein shapes and may consequently not be used for that purpose. However, the linear fit of the PA data to $\Omega = 1.299(\Omega_{PA} - 81\,Å^2)$ shows a maximum of the error distribution at ca. 0.4%. Accordingly, a simple scaling of the PA cross section opens up the possibility to estimate cross sections for protein shapes accurate enough to use under typical laboratory conditions. The reason why this relationship holds is that the shape factor $\rho$ is sharply distributed (see Fig. 6C). This model will be presented in a future publication.

## 12. Summary and conclusions

We introduced and discussed the application of the projected superposition approximation (PSA), a novel algorithm to compute molecular collision cross sections. In the framework of the PSA, molecular collision cross sections are computed as a projection approximation modified to account for collective size and shape effects. These effects are accounted for by a superposition of atomic potentials and by the inclusion of a shape factor. Collision cross sections computed for solid and hollow spheres and cups of fullerene carbon clusters are essentially identical to those determined by the TJM in the temperature range from 80 to 700 K. Here, the PSA model performs clearly better than the EHSS model. The results on carbon clusters with protein shapes demonstrates that the PSA algorithm is able to handle complex molecular shapes as well as the range in molecular size typical to proteins contained in the protein data bank. These results indicate that the PSA is comparable to the TJM in terms of accuracy and outperforms the TJM in terms of computational demand by a factor of 100–1000. Furthermore, our results indicate that PA cross sections can be scaled to accurately yield cross sections for protein shapes. This result will be further explored in a future publication.

## Acknowledgements

We gratefully acknowledge the National Science Foundation under Grant CHE-0909743 and the Air Force Office of Scientific Research for partial support of this work under Grants FA9550-06-1-0069 and FA9550-05-1-0208. Parts of the calculations were carried out at the CNSI Computing Facility at UCSB supported by Hewlett-Packard. C.B. is grateful to the Alexander-von-Humboldt-Foundation for a Feodor-Lynen-Fellowship. We thank Megan Murray Gessel for commenting on the manuscript. The authors are grateful to R.R. Zope for communicating the cartesian coordinates of the fullerenes.

## Appendix A. Supplementary data

Supplementary data associated with this article can be found, in the online version, at doi:10.1016/j.ijms.2011.06.014.

## References

[1] M.T. Bowers, P.R. Kemper, G. von Helden, P.A.M. van Koppen, Science 260 (1993) 1446–1451.
[2] G. von Helden, N.G. Gotts, M.T. Bowers, Nature 363 (1993) 60–63.
[3] G. von Helden, N.G. Gotts, M.T. Bowers, J. Am. Chem. Soc. 115 (1993) 4363–4364.
[4] M.F. Jarrold, J. Phys. Chem. 99 (1995) 11–21.
[5] K.A. Jackson, M. Horoi, I. Chaudhuri, T. Frauenheim, A.A. Shvartsburg, Phys. Rev. Lett. 93 (2004) 013401.

[6] K.M. Ho, A.A. Shvartsburg, B.C. Pan, Z.Y. Lu, C.Z. Wang, J.G. Wacker, J.L. Fye, M.F. Jarrold, Nature 392 (1998) 582–585.
[7] B.T. Ruotolo, J.L.P. Benesch, A.M. Sandercock, S.-J. Hyung, C.V. Robinson, Nat. Protoc. 3 (2008) 1139–1152.
[8] C.S. Hoaglund-Hyzer, A.E. Counterman, D.E. Clemmer, Chem. Rev. 99 (1999) 3037–3079.
[9] A.J.R. Heck, Nat. Methods 5 (2008) 927–933.
[10] T. Wyttenbach, P.R. Kemper, M.T. Bowers, Int. J. Mass Spectrom. 212 (2001) 13–23.
[11] P.R. Kemper, N.F. Dupuis, M.T. Bowers, Int. J. Mass Spectrom. 287 (2009) 46–57.
[12] S.D. Pringle, K. Giles, J.L. Wildgoose, J.P. Williams, S.E. Slade, K. Thalassinos, R.H. Bateman, M.T. Bowers, J.H. Scrivens, Int. J. Mass Spectrom. 261 (2007) 1–12.
[13] D.E. Clemmer, R.R. Hudgins, M.F. Jarrold, J. Am. Chem. Soc. 117 (1995) 10141–10142.
[14] D.E. Clemmer, M.F. Jarrold, J. Mass Spectrom. 32 (1997) 577–592.
[15] T. Wyttenbach, M.T. Bowers, Top. Curr. Chem. 225 (2003) 207–232.
[16] P. Dugourd, R.R. Hudgins, D.E. Clemmer, M.F. Jarrold, Rev. Sci. Instrum. 68 (1997) 1122–1129.
[17] B.T. Ruotolo, K. Giles, I. Campuzano, A.M. Sandercock, R.H. Bateman, C.V. Robinson, Science 310 (2005) 1658–1661.
[18] A.B. Kanu, P. Dwivedi, M. Tam, L. Matz, J.H. Herbert, J. Mass Spectrom. 43 (2008) 1–22.
[19] K. Tang, A.A. Shvartsburg, H.N. Lee, D.C. Prior, M.A. Buschbach, F.M. Li, A.V. Tolmachev, G.A. Anderson, R.D. Smith, Anal. Chem. 77 (2005) 3330–3339.
[20] D.V.D. Spoel, E.G. Marklund, D.S.D. Larsson, C. Caleman, Macromol. Biosci. 11 (2011).
[21] E. Jurneczko, P.E. Barran, Analyst 136 (2010) 20–28.
[22] S.L. Bernstein, N.F. Dupuis, N.D. Lazo, T. Wyttenbach, M.M. Condron, G. Bitan, D.B. Teplow, J.-E. Shea, B.T. Ruotolo, C.V. Robinson, M.T. Bowers, Nat. Chem. 1 (2009) 326–331.
[23] C. Bleiholder, N.F. Dupuis, T. Wyttenbach, M.T. Bowers, Nat. Chem. 3 (2011) 172–177.
[24] C. Uetrecht, I.M. Barbu, G.K. Shoemaker, E.V. Duijn, A.J.R. Heck, Nat. Chem. 3 (2011) 126–132.
[25] C. Uetrecht, R.J. Rose, E.V. Duijn, K. Lorenzen, A.J.R. Heck, Chem. Soc. Rev. 39 (2009) 1633–1655.
[26] T. Wyttenbach, G. von Helden, J.J. Batka, D. Carlat, M.T. Bowers, J. Am. Soc. Mass Spectrom. 8 (1997) 275–282.
[27] M.F. Mesleh, J.M. Hunter, A.A. Shvartsburg, G.C. Schatz, M.F. Jarrold, J. Phys. Chem. A 100 (1996) 16082–16086.
[28] A.A. Shvartsburg, M.F. Jarrold, Chem. Phys. Lett. 261 (1996) 86–91.
[29] A.A. Shvartsburg, B. Liu, M.F. Jarrold, K.M. Ho, J. Chem. Phys. 112 (2000) 4517–4526.
[30] E.A. Mason, E.W. McDaniel, Transport Properties of Ions in Gases, Wiley, New York, 1988.
[31] G. Chalasinski, M.M. Szczesniak, Chem. Rev. 100 (2000) 4227–4252.
[32] B. Jeziorski, R. Moszynski, K. Szalewicz, Chem. Rev. 94 (1994) 1887–1930.
[33] A.J. Misquitta, R. Podeszwa, B. Jeziorski, K. Szalewicz, J. Chem. Phys. 123 (2005) 214103.
[34] C. Bleiholder, D.B. Werz, H. Koppel, R. Gleiter, J. Am. Chem. Soc. 128 (2006) 2666–2674.
[35] Hirschfelder, Curtiss, Bird, Molecular Theory of Gases and Liquids, Wiley, New York, 1954.
[36] A.A. Shvartsburg, B. Liu, K.W.M. Siu, K.M. Ho, J. Phys. Chem. A 104 (2000) 6152–6157.
[37] J.E. Mack, J. Am. Chem. Soc. 47 (1925) 2468–2482.
[38] G. von Helden, M.T. Hsu, N. Gotts, M.T. Bowers, J. Phys. Chem. 97 (1993) 8182–8192.
[39] The Sigma Program, http://bowers.chem.ucsb.edu/theory_analysis/cross-sections/sigma.shtml (accessed 20.06.11).
[40] T. Wyttenbach, J.E. Bushnell, M.T. Bowers, J. Am. Chem. Soc. 120 (1998) 5098–5103.
[41] W.H. Press, S.A. Teukolsky, W.T. Vetterling, B.P. Flannery, Numerical Recipes: The Art of Scientific Computing, 3rd ed., Cambridge University Press, New York, 2007.
[42] C.B. Barber, D.P. Dobkin, H. Huhdanpaa, ACM Trans. Math. Softw. 22 (1996) 469–483.
[43] H. Edelsbrunner, Discrete Comput. Geom. 13 (1995) 415–440.
[44] M. Sanner, A.J. Olson, J.C. Spehner, Biopolymers 38 (1996) 305–320.
[45] J.A. Wilson, A. Bender, T. Kaya, P.A. Clemons, J. Chem. Inf. Model. 49 (2009) 2231–2241.
[46] B. Lee, F.M. Richards, J. Mol. Biol. 55 (1971) 379–400.
[47] I.M. Sobol, U. S. S. R. Comput. Maths. Math. Phys. 7 (1967) 86–112.
[48] P. Jaeckel, Monte Carlo Methods in Finance, Wiley, 2002.
[49] M. Matsumoto, T. Nishimura, ACM Trans. Model. Comput. Simul. 8 (1998) 3–30.
[50] R.R. Zope, T. Baruah, M.R. Pederson, B.I. Dunlap, Phys. Rev. B 77 (2008) 115452.
[51] G. von Helden, T. Wyttenbach, M.T. Bowers, Science 267 (1995) 1483–1485.
[52] A.A. Shvartsburg, G.C. Schatz, M.F. Jarrold, J. Chem. Phys. 108 (1998) 2416–2423.